



MIT Open Access Articles

Structures and topological defects in pressure-driven lyotropic chromonic liquid crystals

The MIT Faculty has made this article openly available. **Please share** how this access benefits you. Your story matters.

Citation	Zhang, Qing, Zhang, Rui, Ge, Baoliang, Yaqoob, Zahid, So, Peter TC et al. 2021. "Structures and topological defects in pressure-driven lyotropic chromonic liquid crystals." Proceedings of the National Academy of Sciences, 118 (35).
As Published	10.1073/pnas.2108361118
Publisher	Proceedings of the National Academy of Sciences
Version	Final published version
Citable link	https://hdl.handle.net/1721.1/138472
Terms of Use	Article is made available in accordance with the publisher's policy and may be subject to US copyright law. Please refer to the publisher's site for terms of use.

Structures and topological defects in pressure-driven lyotropic chromonic liquid crystals

Qing Zhang^{a,1} , Rui Zhang^{b,1}, Baoliang Ge^{a,c,1}, Zahid Yaqoob^c , Peter T. C. So^{a,c,d} , and Irmgard Bischofberger^{a,2} 

^aDepartment of Mechanical Engineering, Massachusetts Institute of Technology, Cambridge, MA 02139; ^bDepartment of Physics, The Hong Kong University of Science and Technology, Hong Kong, China; ^cLaser Biomedical Research Center, Massachusetts Institute of Technology, Cambridge, MA 02139; and ^dDepartment of Biological Engineering, Massachusetts Institute of Technology, Cambridge, MA 02139

Edited by Tom C. Lubensky, University of Pennsylvania, Philadelphia, PA, and approved July 23, 2021 (received for review May 6, 2021)

Lyotropic chromonic liquid crystals are water-based materials composed of self-assembled cylindrical aggregates. Their behavior under flow is poorly understood, and quantitatively resolving the optical retardance of the flowing liquid crystal has so far been limited by the imaging speed of current polarization-resolved imaging techniques. Here, we employ a single-shot quantitative polarization imaging method, termed polarized shearing interference microscopy, to quantify the spatial distribution and the dynamics of the structures emerging in nematic disodium cromoglycate solutions in a microfluidic channel. We show that pure-twist disclination loops nucleate in the bulk flow over a range of shear rates. These loops are elongated in the flow direction and exhibit a constant aspect ratio that is governed by the nonnegligible splay-bend anisotropy at the loop boundary. The size of the loops is set by the balance between nucleation forces and annihilation forces acting on the disclination. The fluctuations of the pure-twist disclination loops reflect the tumbling character of nematic disodium cromoglycate. Our study, including experiment, simulation, and scaling analysis, provides a comprehensive understanding of the structure and dynamics of pressure-driven lyotropic chromonic liquid crystals and might open new routes for using these materials to control assembly and flow of biological systems or particles in microfluidic devices.

lyotropic chromonic liquid crystals | pressure-driven flow of nematics | topological defects | pure-twist disclination loops | polarized shearing interference microscopy

L yotropic chromonic liquid crystals (LCLCs) are aqueous dispersions of organic disk-like molecules that self-assemble into cylindrical aggregates, which form nematic or columnar liquid crystal phases under appropriate conditions of concentration and temperature (1–6). These materials have gained increasing attention in both fundamental and applied research over the past decade, due to their distinct structural properties and biocompatibility (4, 7–14). Used as a replacement for isotropic fluids in microfluidic devices, nematic LCLCs have been employed to control the behavior of bacteria and colloids (13, 15–20).

Nematic liquid crystals form topological defects under flow, which gives rise to complex dynamical structures that have been extensively studied in thermotropic liquid crystals (TLCs) and liquid crystal polymers (LCPs) (21–29). In contrast to lyotropic liquid crystals that are dispersed in a solvent and whose phase can be tuned by either concentration or temperature, TLCs do not need a solvent to possess a liquid-crystalline state and their phase depends only on temperature (30). Most TLCs are shear-aligned nematics, in which the director evolves toward an equilibrium out-of-plane polar angle. Defects nucleate beyond a critical Ericksen number due to the irreconcilable alignment of the directors from surface anchoring and shear alignment in the bulk flow (24, 31–33). With an increase in shear rate, the defect type can transition from π -walls (domain walls that separate regions whose director orientation differs by an angle of π)

to ordered disclinations and to a disordered chaotic regime (34). Recent efforts have aimed to tune and control the defect structures by understanding the relation between the selection of topological defect types and the flow field in flowing TLCs. Strategies to do so include tuning the geometry of microfluidic channels, inducing defect nucleation through the introduction of isotropic phases or designing inhomogeneities in the surface anchoring (35–39). LCPs are typically tumbling nematics for which $\alpha_2\alpha_3 < 0$, where α_2 and α_3 are the Leslie viscosities. This leads to a nonzero viscous torque for any orientation of the director, which allows the director to rotate in the shear plane (22, 29, 30, 40). The tumbling character of LCPs facilitates the nucleation of singular topological defects (22, 40). Moreover, the molecular rotational relaxation times of LCPs are longer than those of TLCs, and they can exceed the timescales imposed by the shear rate. As a result, the rheological behavior of LCPs is governed not only by spatial gradients of the director field from the Frank elasticity, but also by changes in the molecular order parameter (25, 41–43). With increasing shear rate, topological defects in LCPs have been shown to transition from disclinations to rolling cells and to worm-like patterns (25, 26, 43).

Topological defects occurring in the flow of nematic LCLCs have so far received much more limited attention (44, 45). At rest, LCLCs exhibit unique properties distinct from those of TLCs and LCPs (1, 2, 4–6, 44). In particular, LCLCs have significant elastic anisotropy compared to TLCs; the twist Frank elastic constant, K_2 , is much smaller than the splay and bend

Significance

Many driven and active nematic fluids exhibit complex microstructures, but their characteristics and dynamics are poorly understood. We explore the structures emerging in a pressure-driven nematic lyotropic chromonic liquid crystal in a microfluidic channel. We show that twist-type topological defects spontaneously emerge under flow. Our single-shot quantitative polarization imaging method allows us to quantify the fluctuations of these defects, which we show to reflect the tumbling character of the liquid crystal. We report how the defect size is governed by the balance between nucleation and annihilation forces, a balance that can be tuned by the flow rate. Such control over the microstructure opens pathways for using these nematic materials in optical devices and to control assembly of biological systems.

Author contributions: Q.Z., B.G., P.T.C.S., and I.B. designed research; R.Z. developed computational models; Q.Z., R.Z., and B.G. performed research; Q.Z., R.Z., B.G., Z.Y., P.T.C.S., and I.B. analyzed data; and Q.Z., R.Z., B.G., P.T.C.S., and I.B. wrote the paper.

The authors declare no competing interest.

This article is a PNAS Direct Submission.

Published under the PNAS license.

¹Q.Z., R.Z., and B.G. contributed equally to this work.

²To whom correspondence may be addressed. Email: irmgard@mit.edu.

This article contains supporting information online at <https://www.pnas.org/lookup/suppl/doi:10.1073/pnas.2108361118/-DCSupplemental>.

Published August 26, 2021.

Frank elastic constants, K_1 and K_3 . The resulting relative ease with which twist deformations can occur can lead to a spontaneous symmetry breaking and the emergence of chiral structures in static LCLCs under spatial confinement, despite the achiral nature of the molecules (4, 46–51). When driven out of equilibrium by an imposed flow, the average director field of LCLCs has been reported to align predominantly along the shear direction under strong shear but to reorient to an alignment perpendicular to the shear direction below a critical shear rate (52–54). A recent study has revealed a variety of complex textures that emerge in simple shear flow in the nematic LCLC disodium cromoglycate (DSCG) (44). The tumbling nature of this liquid crystal leads to enhanced sensitivity to shear rate. At shear rates $\dot{\gamma} < 1 \text{ s}^{-1}$, the director realigns perpendicular to the flow direction adapting a so-called log-rolling state characteristic of tumbling nematics. For $1 \text{ s}^{-1} < \dot{\gamma} < 10 \text{ s}^{-1}$, polydomain textures form due to the nucleation of pure-twist disclination loops, for which the rotation vector is parallel to the loop normal, and mixed wedge-twist disclination loops, for which the rotation vector is perpendicular to the loop normal (44, 55). Above $\dot{\gamma} > 10 \text{ s}^{-1}$, the disclination loops gradually transform into periodic stripes in which the director aligns predominantly along the flow direction (44).

Here, we report on the structure and dynamics of topological defects occurring in the pressure-driven flow of nematic DSCG. A quantitative evaluation of such dynamics has so far remained challenging, in particular for fast flow velocities, due to the slow image acquisition rate of current quantitative polarization-resolved imaging techniques. Quantitative polarization imaging traditionally relies on three commonly used techniques: fluorescence confocal polarization microscopy, polarizing optical microscopy, and LC-PolScope imaging. Fluorescence confocal polarization microscopy can provide accurate maps of birefringence and orientation angle, but the fluorescent labeling may perturb the flow properties (56). Polarizing optical microscopy requires a mechanical rotation of the polarizers and multiple measurements, which severely limits the imaging speed. LC-PolScope, an extension of conventional polarization optical microscopy, utilizes liquid crystal universal compensators to replace the compensator used in conventional polarization microscopes (57). This leads to an enhanced imaging speed and better compensation for polarization artifacts of the optical system. The need for multiple measurements to quantify retardance, however, still limits the acquisition rate of LC-PolScopes.

We overcome these challenges by using a single-shot quantitative polarization microscopy technique, termed polarized shearing interference microscopy (PSIM). PSIM combines circular polarization light excitation with off-axis shearing interferometry detection. Using a custom polarization retrieval algorithm, we achieve single-shot mapping of the retardance, which allows us to reach imaging speeds that are limited only by the camera frame rate while preserving a large field-of-view and micrometer spatial resolution. We provide a brief discussion of the optical design of PSIM in *Materials and Methods*; further details of the measurement accuracy and imaging performance of PSIM are reported in ref. 58.

Using a combination of experiments, numerical simulations and scaling analysis, we show that in the pressure-driven flow of nematic DSCG solutions in a microfluidic channel, pure-twist disclination loops emerge for a certain range of shear rates. These loops are elongated in the flow with a fixed aspect ratio. We demonstrate that the disclination loops nucleate at the boundary between regions where the director aligns predominantly along the flow direction close to the channel walls and regions where the director aligns predominantly perpendicular to the flow direction in the center of the channel. The large elastic stresses of the director gradient at the boundary are then

released by the formation of disclination loops. We show that both the characteristic size and the fluctuations of the pure-twist disclination loops can be tuned by controlling the flow rate.

Results and Discussion

Emerging Structures in Pressure-Driven Flow of Nematic DSCG Solutions. We inject an aqueous solution of 13 wt% DSCG into a rectangular microfluidic channel of length $l = 50 \text{ mm}$, width $w = 15 \text{ mm}$, and thickness $b = 6.5 \pm 1 \text{ }\mu\text{m}$. At this concentration, DSCG is in the nematic phase at room temperature $T = 22.5 \pm 0.5 \text{ }^\circ\text{C}$ (59, 60). The optical birefringence of 13 wt% DSCG at rest, $\Delta n = n_e - n_o$, is -0.015 at a wavelength $\lambda_w = 633 \text{ nm}$, where n_e and n_o are the extraordinary and ordinary refractive indices (61). The corresponding maximum retardance, $\Gamma_{\text{max}} = \frac{2\pi}{\lambda_w} \Delta n b$, is $0.98 \pm 0.15 \text{ rad}$. The liquid crystal is initially planar aligned along the direction of the flow (*Materials and Methods*). The flow is induced by injecting DSCG solutions at a volumetric flow rate q , ranging from $q = 0.07$ – $25 \text{ }\mu\text{L/min}$, controlled by a syringe pump (Harvard PHD 2000). The corresponding Ericksen numbers $\text{Er} = \frac{\eta_2 \dot{\gamma} b^2}{K_2}$ vary from 306 to 109,267, where Er characterizes the relative importance of the viscous forces to the elastic forces. Here, η_2 is the twist viscosity, K_2 is the twist Frank elastic constant, and $\dot{\gamma} = q/(wb^2)$ is the average shear rate (5, 59).

Distinct structures emerge in the material upon the onset of the pressure-driven flow, as shown in the snapshots in Fig. 1A, which are imaged in polarizing optical microscopy with a static full-wave-plate optical compensator (560 nm) with the slow axis oriented at 45° to the crossed polarizers and in the direction parallel to the flow. Orange colors indicate that the director is parallel to the flow direction (x direction), and blue colors indicate that the director is perpendicular to the flow direction (61). At low flow rate, DSCG is preferentially aligned perpendicular to the flow, adopting a log-rolling state with in-plane orientation angle $\varphi = 90^\circ$, even though before the onset of flow the director is parallel to the flow direction $\varphi = 0^\circ$ (Fig. 1B). This realignment of the director is a consequence of the tumbling character of DSCG and the significant anisotropy in the splay Frank elastic constant K_1 and twist Frank elastic constant K_2 , where $K_1/K_2 \approx 10$; the director reorients by a twist deformation toward the y axis, instead of deforming in the shear plane, which would involve splay deformations (44, 62). With an increase in flow rate, domains appear where the director increasingly aligns in the direction of the flow. The characteristic size of these domains becomes systematically smaller with increasing flow rate.

To quantify these structures, we use PSIM to obtain a map of the effective optical retardance, as shown in Fig. 1C where the colors represent the value of the optical retardance averaged over the thickness of the channel (z direction). We determine the characteristic size of the domains of varying retardance by calculating the normalized two-dimensional (2D) spatial autocovariance in the x and y directions, C_x and C_y , as shown in Fig. 2A (see *SI Appendix* for details) (63). The observed decrease in domain size with increasing flow rate is reflected in a decay of the autocovariance at increasingly smaller Δx and Δy , which denote the shift in the x and y directions, respectively. For the two lowest and the highest flow rates probed, C_x and C_y exhibit a two-step decay suggesting a coexistence of structures of two characteristic sizes. We use a double compressed exponential fit to access the characteristic length scales L_{x1} , L_{x2} , L_{y1} , and L_{y2} , characterizing the average sizes of structures along the x and y directions. For the intermediate range of flow rates, we fit C_x and C_y with a single compressed exponential function, which yields L_x and L_y . Details on the fits and fit parameters are provided in *SI Appendix, text and Table S1*. Remarkably, L_x and L_y decrease monotonically with the average shear rate

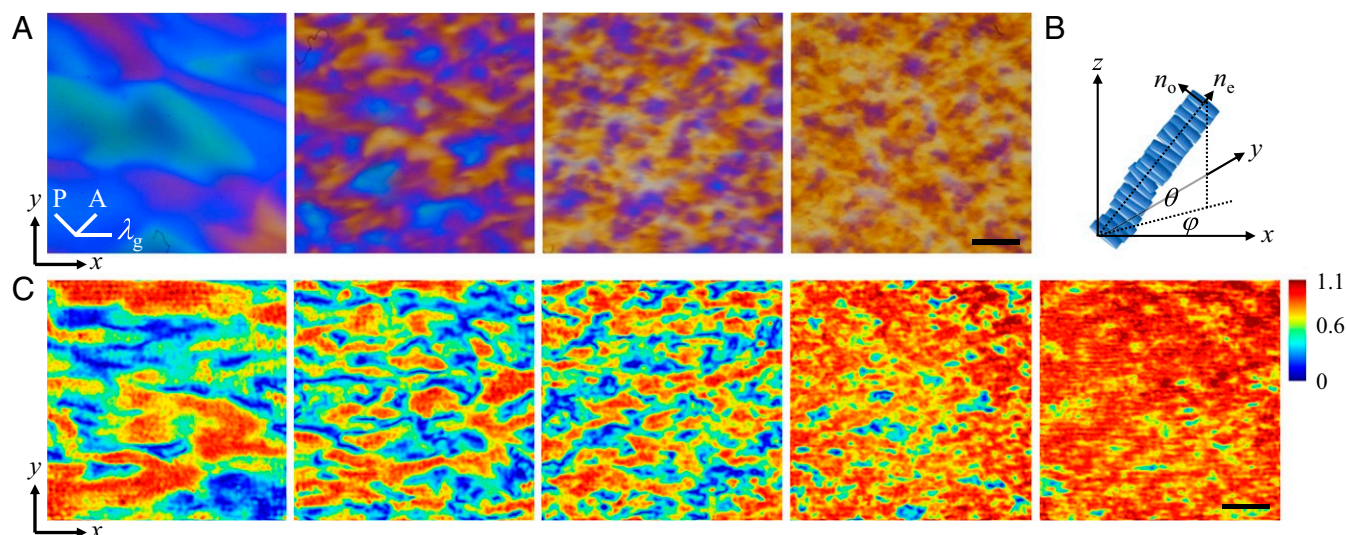


Fig. 1. Flow-induced structures in nematic DSCG solutions. (A) Structures observed in polarizing optical microscopy for (from Left to Right): $q = 0.07 \mu\text{L/min}$, $0.2 \mu\text{L/min}$, $0.5 \mu\text{L/min}$, and $3 \mu\text{L/min}$, using a full-wave-plate optical compensator with its slow axis, λ_g , aligned parallel to the flow direction. The flow is in the x direction; the height of the microfluidic channel is in the z direction. A denotes the analyzer and P denotes the polarizer. (B) Schematic of the director orientation. n_e is the extraordinary refractive index; n_o is the ordinary refractive index. The in-plane orientation angle (azimuthal angle) and out-of-plane orientation angle (polar angle) are φ and θ . (C) Retardance maps obtained from PSIM images for (from Left to Right): $q = 0.07 \mu\text{L/min}$, $0.2 \mu\text{L/min}$, $0.5 \mu\text{L/min}$, $3 \mu\text{L/min}$, and $25 \mu\text{L/min}$. The color represents the optical retardance. Scale bars: A and C, $50 \mu\text{m}$.

for $4 \text{ s}^{-1} < \bar{\gamma} < 500 \text{ s}^{-1}$, as displayed in Fig. 2B. The average characteristic size, defined as $L = \sqrt{L_x L_y}$, exhibits a power-law dependence with the shear rate, $L \propto \bar{\gamma}^{-0.19}$. The domains are elongated in the flow direction, with an approximately constant aspect ratio $L_x/L_y = 1.8 \pm 0.3$, as shown in Fig. 2C. A decrease or an increase in shear rate leads to different characteristics of the domain sizes and the aspect ratio. We focus our discussion on the intermediate range of shear rates.

Structures Represent Pure-Twist Disclination Loops. To identify the nature of the structures, we need to understand the observed changes in the optical retardance, which could be attributed to three possible effects: 1) changes of the out-of-plane orientation angle θ , 2) changes of the order parameter at topological defects, or 3) twist deformations along the z direction (44). To reveal the dominant effect leading to the observed retardance

and the nature of the structures formed in DSCG solutions, we perform hydrodynamic simulations of tumbling nematic liquid crystals using a hybrid lattice Boltzmann method, which allows us to access the director field for Ericksen numbers $\text{Er} = \frac{\eta_2 \bar{\gamma} b^2}{K_2}$ varying from 579 to 8,214, a range which overlaps with the lower flow rates probed in the experiments. At $\text{Er} < 2,480$, the directors are predominantly aligned perpendicular to the flow direction (see *SI Appendix, text and Fig. S1* for details). With increasing Er , the directors gradually reorient toward the flow direction. Disclination loops nucleate in the flow, shown as blue lines denoting isosurfaces of order parameter 0.35 in Fig. 3A for $\text{Er} = 7,438$, where the dark rods denote the director field in the plane of the loop. To link the simulations to the experiments, we calculate the effective optical retardance averaged over the channel thickness, as shown in Fig. 3B (*SI Appendix*). This reveals that the low retardance regions correspond to disclination loops. The majority of

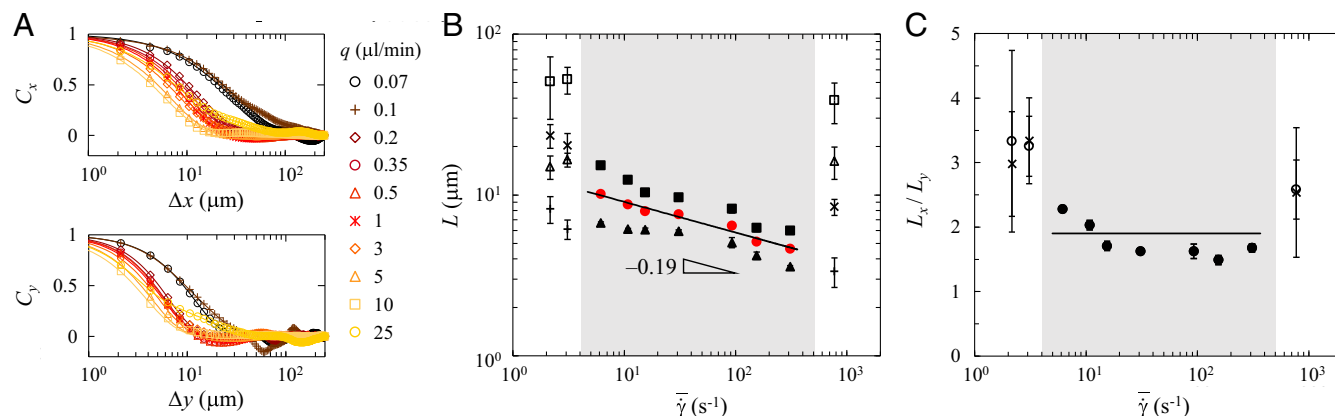


Fig. 2. Characteristic size of structures in flowing DSCG solutions controlled by average shear rate. (A) Normalized 2D spatial autocovariance in the x direction (Top) and in the y direction (Bottom), for different flow rates q . The solid lines denote compressed single or double exponential fits. (B) Characteristic domain sizes versus average shear rate $\bar{\gamma}$. Along the x direction for intermediate average flow rates, L_x (■), and for low and high average flow rates, L_{x1} (□), L_{x2} (×); along the y direction for intermediate flow rates, L_y (▲), and for low and high flow rates, L_{y1} (△), L_{y2} (+); and the average characteristic size $L = \sqrt{L_x L_y}$ (●). The black line denotes $L \propto \bar{\gamma}^{-0.19}$. (C) Aspect ratio L_x/L_y (●) for intermediate average flow rates, and L_{x1}/L_{y1} (○) and L_{x2}/L_{y2} (×) for low and high average flow rates. The black line indicates $L_x/L_y \approx \sqrt{K_3/K_1} = 1.9$. In B and C, some of the error bars are smaller than the symbols.

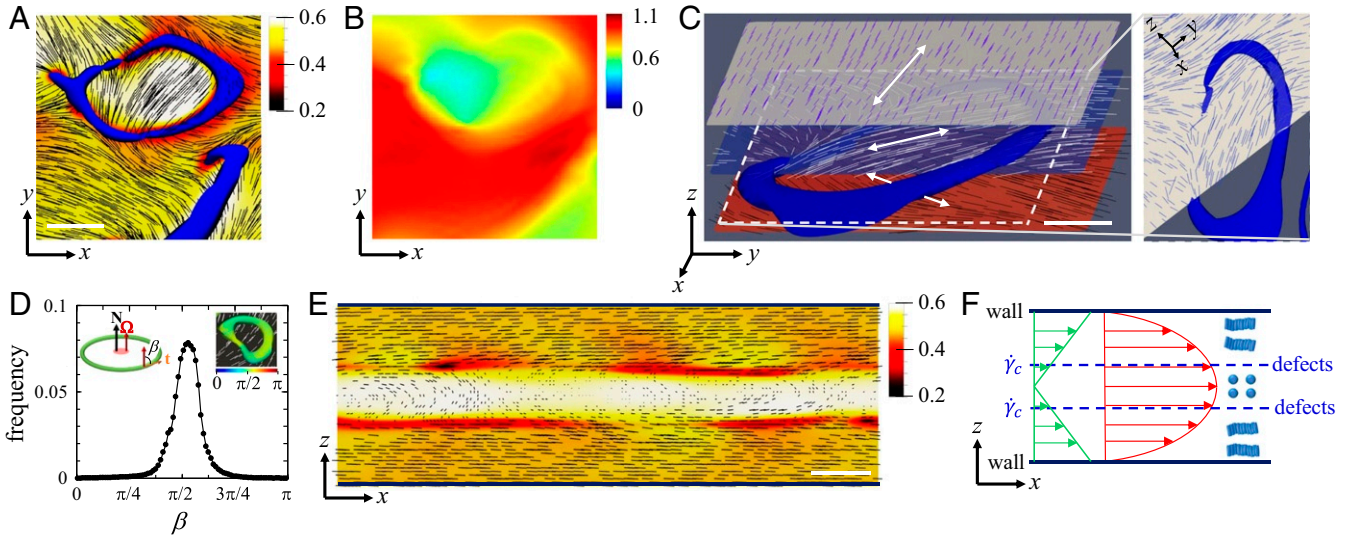


Fig. 3. Simulations of the director field in pressure-driven flow for $Er = 7,438$. (A) Top view of a disclination loop (blue isosurface of order parameter 0.35). The loop is located in the xy plane. The dark rods denote the directors in the plane of the disclination loop. The color bar denotes the value of the scalar order parameter. The scale bar corresponds to $3 \mu\text{m}$ in the experiment. (B) Map of the optical retardance averaged along the z axis and determined from the director field. (C) Structure of a pure-twist disclination loop (blue isosurface). The arrows indicate the local buildup of the twist distortion. Scale bar: $2 \mu\text{m}$. (D) Probability distribution of the twist angle β extracted from ~ 100 loops in the simulations. β is the angle between the rotation vector Ω and the local tangent vector \mathbf{t} of a disclination loop (Left Inset). β is close to $\pi/2$, which reveals the prevalence of twist winding. (Right Inset) The coloring of the disclination loop indicates the twist angle β . (E) Cross-section along the flow direction. The directors align perpendicular to the flow direction in the center of the channel and parallel to the flow direction near the channel walls. The defects predominantly nucleate at the interface between these two regions. Scale bar: $2 \mu\text{m}$. (F) Schematics indicating the log-rolling layer ($\dot{\gamma} < \dot{\gamma}_c$), the layers aligned in the flow direction ($\dot{\gamma} > \dot{\gamma}_c$), and the location of defects. The red arrows schematically represent the velocity profile; the green arrows represent the shear rate profile $\dot{\gamma}$.

the disclination loops are topologically neutral pure-twist disclination loops, where the rotation vector is parallel to the normal direction of the loop (55), as shown in Fig. 3C.

We can rationalize the formation of pure-twist disclination loops by considering the elastic powers of splay, twist, and bend deformations, which can be expressed as $P_{\text{splay}} = \int_{\Lambda} d\Lambda (\nabla \cdot \mathbf{n})^2$, $P_{\text{twist}} = \int_{\Lambda} d\Lambda (\mathbf{n} \cdot \nabla \times \mathbf{n})^2$, and $P_{\text{bend}} = \int_{\Lambda} d\Lambda (\mathbf{n} \times \nabla \times \mathbf{n})^2$, where Λ is a control volume. The simulations indeed show that P_{twist} is larger than the powers associated with splay and bend modes (SI Appendix, Fig. S2). Therefore, even though the tumbling property of DSCG allows for the formation of wedge disclinations (44), twist-type defects are dominant in pressure-driven flow. To further quantify the prevalence of pure-twist disclination loops, we determine the local winding of the director field along the loop, which is characterized by the twist angle β between the rotation vector Ω and the local tangent vector \mathbf{t} of a disclination loop (Fig. 3D, Inset). A value of $\beta = \pi/2$ denotes a local twist winding; a value of $\beta = 0$ or π denotes a local $\pm 1/2$ wedge winding (55). For a pure-twist disclination loop, the distribution of β is a delta function with $\beta = \pi/2$ everywhere along the loop. A wedge-twist disclination loop, by contrast, is characterized by a β that continuously varies from 0 to π and back to 0 upon one full revolution around the loop (see SI Appendix, text and Fig. S3 for details). The distribution of β measured for the disclination loops emerging in the flow of DSCG solutions exhibits a peak at $\beta = \pi/2$, as shown in Fig. 3D, which reveals that pure-twist disclination loops are indeed prevalent compared to wedge-twist disclination loops. This is further evidenced by the finding that the rotation vector Ω is almost uniformly parallel to the loop normal \mathbf{N} (SI Appendix, text and Fig. S4). The emergence of pure-twist disclination loops is a consequence of the smallness of the twist Frank elastic constant, which favors the local buildup of twist distortions in the z direction, from which the loops nucleate (30, 44, 64).

The pure-twist disclination loops form at the boundary between two regions of irreconcilable director alignments: Close

to the two channel walls, the directors are aligned in the shear plane, while in a region at the center of the channel the directors adopt a log-rolling state, as shown in Fig. 3E. Due to the high stored energy in the director gradient at the interface between these two frustrated regions, the elastic stress is released by forming topological defects. This complex director field within the channel gap results from the tumbling character of DSCG and the nonuniform shear rate across the gap; DSCG is in a log-rolling state below a critical shear rate $\dot{\gamma}_c$, but rotates toward the shear plane above $\dot{\gamma}_c$ (44, 54), as schematically shown in Fig. 3F.

To understand the transition to a different regime of flow structures at lower shear rates, we note that twist deformations can, a priori, lead to two types of topological defects: twist walls aligned parallel to the xy plane, and pure-twist disclination loops (55, 64). The energy required to form a twist wall is $E_{\text{twist wall}} \approx 0.4 L_w b \sqrt{-\alpha_2 K_2 \dot{\gamma}}$, where L_w is the length of the twist wall, $K_2 \approx 0.4 \text{ pN}$ is the twist Frank elastic constant, and $\alpha_2 \approx -1.66 \text{ Pa}\cdot\text{s}$ is the Leslie viscosity coefficient for 13 wt% DSCG solutions (59) (see SI Appendix for details). The energy required to form a pure-twist disclination loop is $E_{\text{pure-twist}} = \frac{\pi}{4} K_2 L_p \ln(\frac{L}{a})$ (64), where L_p and L are the perimeter and the diameter of a pure-twist disclination loop, respectively, and a is the diameter of the defect core in the nematic phase, which we estimate to be approximately $0.1 \mu\text{m}$. Pure-twist disclination loops rather than twist walls form when $E_{\text{pure-twist}} < E_{\text{twist wall}}$; this condition is reached for a critical shear rate $\dot{\gamma}^* \approx 0.8 \text{ s}^{-1}$. Considering the nonuniform shear rates across the thickness of the channel, twist walls become negligible when the shear rate in the center region [within a nematic coherence length $\approx a$ (30)] reaches 0.8 s^{-1} , which corresponds to a critical average shear rate $\bar{\dot{\gamma}}^* = \frac{\dot{\gamma}^* b}{12a} \approx 4 \text{ s}^{-1}$. This value indeed denotes the onset of the intermediate shear rate regime in Fig. 2B.

Characteristic Size and Aspect Ratio of Pure-Twist Disclination Loops. Having established the emergence of pure-twist disclination loops in the range of intermediate average shear rates now

allows us to rationalize the observed power-law dependence of $L \propto \bar{\gamma}^{-0.19}$. To do so, we consider the nucleation forces and annihilation forces acting on the loop. The nonuniform twist deformation across the gap favors the nucleation; the viscous force imposed by the flow acts to annihilate the nucleated defects. The energy input to nucleate N pure-twist disclination loops is $E_n = N E_{\text{pure-twist}}$. Simulations have determined that the number of nucleated twist defects at a given time induced by shear flow scales as $N \propto (\text{Er} - \text{Er}_c)^{0.5}$ (65), where Er_c is the critical Ericksen number above which defects nucleate and $\text{Er} = \frac{\eta_2 \dot{\gamma} b^2}{K_2}$ is the Ericksen number that governs the nucleation of twist-type defects. We here set $(\text{Er} - \text{Er}_c)^{0.5} \approx \text{Er}^{0.5}$, as we focus on the range where $\text{Er} \gg \text{Er}_c$. This then yields the nucleation energy per unit volume as $e_n = E_n/\Lambda \propto \frac{1}{\Lambda} \left(\frac{\eta_2 \dot{\gamma} b^2}{K_2} \right)^{0.5} K_2 L_p \ln \left(\frac{L}{a} \right)$, where Λ is a control volume. The annihilation of pure-twist disclination loops is driven by the viscous force and resisted by the elasticity, and can be expressed as the sum of the viscous forces and the elastic forces in a control volume Λ : $f_a = \frac{1}{\Lambda} \left(\int \eta_2 \dot{\gamma} dS + K_2 \right)$, where $\int dS \propto L^2$ is the area occupied by a twist loop of size L . For our range of intermediate average shear rates, $\text{Er} \gg 1$, indicating that viscous effects dominate, thus $f_a \propto \frac{\eta_2 \dot{\gamma} L^2}{\Lambda}$. Balancing the nucleation and annihilation forces, $\frac{de_n}{dL} + f_a = 0$, gives an expression for the average characteristic size of the disclination loops:

$$L \propto \left(\frac{K_2}{\eta_2} \right)^{0.25} b^{0.5} \bar{\gamma}^{-0.25}. \quad [1]$$

This scaling argument indeed yields a power-law exponent for $\bar{\gamma}$ fairly close to that observed in experiments, $L \propto \bar{\gamma}^{-0.19}$. The characteristic loop size is thus governed by a balance between the nucleation force and the annihilation force acting on the loop.

We can likewise understand the aspect ratio of the pure-twist disclination loops, $L_x/L_y \approx 1.8 \pm 0.3$, as being due to the asymmetric elastic deformation that results from the nonnegligible splay-bend anisotropy of DSCG. We consider the aspect ratio to be dominated by the elastic relaxation related to the deformation of the director field at the boundary of the disclination loop. This is a justified assumption given that the timescales related to the loop fluctuations induced by the viscous torque are much shorter than those characterizing the elastic deformation. The director field within the plane of a pure-twist disclination loop is described by $\mathbf{n} = (\cos \theta \cos \varphi, \cos \theta \sin \varphi, \sin \theta)$, where $\theta = 0^\circ$. The director field outside the loop is uniform and predominantly along the x direction, so that φ is a small angle close to 0° . Inside the loop, the director field is likewise uniform, but $\varphi > 0$. With these assumptions, and realizing that the deformation at the boundary of a pure-twist disclination loop along the x direction involves bend deformations, while that along the y direction involves splay deformations, the nematodynamic equation (30, 64) along the x direction then reads as follows (see [SI Appendix](#) for details):

$$K_3 \frac{\partial^2 \varphi}{\partial x^2} + K_2 \frac{\partial^2 \varphi}{\partial z^2} = \gamma_1 \frac{d\varphi}{dt}, \quad [2]$$

and along the y direction:

$$K_1 \frac{\partial^2 \varphi}{\partial y^2} + K_2 \frac{\partial^2 \varphi}{\partial z^2} = \gamma_1 \frac{d\varphi}{dt}, \quad [3]$$

where γ_1 is the rotational viscosity, $\frac{\partial^2 \varphi}{\partial x^2} \propto \frac{1}{L_x^2}$, $\frac{\partial^2 \varphi}{\partial y^2} \propto \frac{1}{L_y^2}$, and $\frac{\partial^2 \varphi}{\partial z^2} \propto \frac{1}{b^2}$. We interrogate the characteristic length scales in the x and y directions related to the spatial gradient of the director field within a certain time window. The time scales related to the elastic deformation in the x and y directions then scale as $\Delta t_x \propto$

$\left(\frac{\gamma_1}{\frac{K_3}{L_x^2} + \frac{K_2}{b^2}} \right)$ and $\Delta t_y \propto \left(\frac{\gamma_1}{\frac{K_1}{L_y^2} + \frac{K_2}{b^2}} \right)$, respectively. With $K_1, K_3 \gg K_2$ (5), this simplifies to $\Delta t_x \propto \frac{\gamma_1 L_x^2}{K_3}$ and $\Delta t_y \propto \frac{\gamma_1 L_y^2}{K_1}$. At steady state, $\Delta t_x = \Delta t_y$, which yields the following:

$$\frac{L_x}{L_y} \approx \sqrt{\frac{K_3}{K_1}} = 1.9. \quad [4]$$

The value of 1.9 is in good agreement with the experimentally determined value of 1.8 ± 0.3 .

Dynamics of Pure-Twist Disclination Loops. Our single-shot imaging technique PSIM allows us to resolve the dynamics of the pure-twist disclination loops. We calculate the normalized spatiotemporal autocovariance, C_t , which contains the coupled information of two contributions: the fluctuations of the disclination loops characterized by a fluctuation time τ_1 and the translation of the disclination loops imposed by the background flow characterized by a translation time τ_2 . To remove the contribution from the background flow, we need to place ourselves in the frame of reference of the disclination loop. In this Lagrangian framework, we move the region of interest by $\Delta x = V_f \Delta t$ at each time lag Δt , where V_f is the velocity of the frame of reference. Only if V_f is equal to the center of mass velocity of the disclination loop, V^* , we access the fluctuations. In our pressure-driven flow, the flow velocity varies across the thickness of the channel. As the location of the pure-twist disclination loops within the channel is unknown, V^* is unknown. We thus calculate C_t for different frame of reference velocities, as shown in Fig. 4A for V_f equal to the average velocity across the channel \bar{V} , and determine the characteristic time τ by fitting to a stretched exponential function (details on the fit and fit parameters are provided in [SI Appendix, text and Table S2](#)). The relation between the fluctuation time τ_1 , the translation time τ_2 , and the characteristic time τ can be expressed as follows (see [SI Appendix](#) for details):

$$\frac{1}{\tau} = \frac{1}{\tau_1} + \frac{1}{\tau_2}, \quad [5]$$

where $\frac{1}{\tau_2} = \frac{|V^* - V_f|}{L_x}$ with L_x the characteristic length scale along the x direction. This expression indeed well describes the dependence of τ^{-1} on V_f/\bar{V} , as shown in Fig. 4B for different flow rates. The frame of reference velocity V_f at which τ^{-1} reaches a minimum denotes the center of mass velocity, V^* , which is between 1.1 and 1.4 \bar{V} . This indicates that the disclination loops are located in the bulk flow rather than near the channel walls, in agreement with our simulations. Fitting τ^{-1} with Eq. 5 yields the fluctuation time τ_1 and the characteristic length scale along the x direction, L_x , as shown in Fig. 4C. The agreement between L_x from this fit and L_x from the normalized spatial autocovariance validates our approach. The fluctuation time τ_1 scales as $1/\bar{\gamma}$. To understand this dependence, we consider the nematodynamic equations for the director field $\mathbf{n} = (\cos \theta \cos \varphi, \cos \theta \sin \varphi, \sin \theta)$. Given the high Ericksen number regime of our experiments, we here neglect the elastic contributions (30, 64):

$$\gamma_1 \cos \theta \dot{\varphi} = -\alpha_2 \sin \theta \sin \varphi \dot{\gamma}, \quad [6]$$

$$\gamma_1 \dot{\theta} = (\alpha_2 \sin^2 \theta - \alpha_3 \cos^2 \theta) \cos \varphi \dot{\gamma}, \quad [7]$$

where α_2 and α_3 are the Leslie viscosity coefficients, and γ_1 is the rotational viscosity. We account for the tumbling character of nematic DSCG solutions by considering small out-of-plane perturbations θ_1 and in-plane perturbations φ_1 for directors aligned perpendicular to the flow direction: $\theta = \theta_1$ and $\varphi = \frac{\pi}{2} + \varphi_1$.

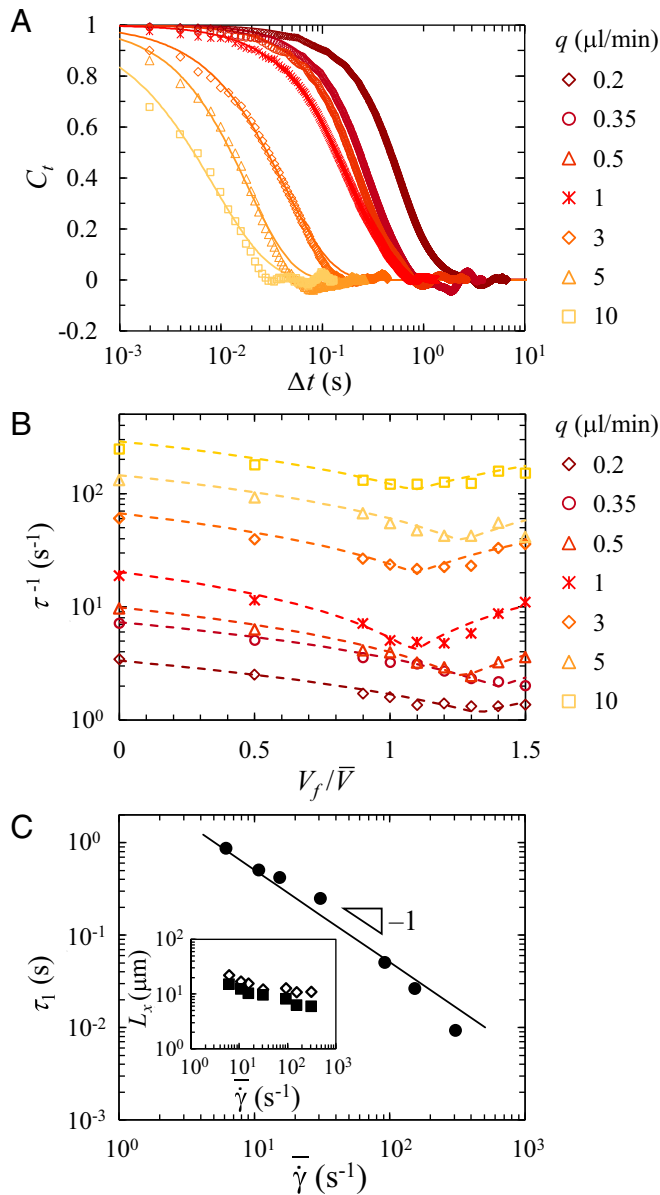


Fig. 4. Dynamics of pure-twist disclination loops. (A) Normalized spatiotemporal autocovariance for different flow rates q , for a frame of reference velocity V_f equal to the average velocity \bar{V} . The lines denote stretched/compressed exponential fits. (B) Inverse characteristic time, τ^{-1} , versus V_f/\bar{V} for different flow rates q . The dashed lines denote best fits to Eq. 5. (C) The fluctuation time τ_1 decreases linearly with the average shear rate. The black line denotes $\tau_f \approx \frac{3}{4} \frac{\gamma_1}{\sqrt{-\alpha_2 \alpha_3}} \frac{1}{\dot{\gamma}}$. (Inset) Comparison between L_x from fitting τ^{-1} (\diamond) and L_x from fitting the normalized spatial autocovariance (\blacksquare).

Linearizing Eqs. 6 and 7 in terms of these perturbations yields a characteristic fluctuation time of the tumbling nematics: $\tau_f \approx \frac{3}{4} \frac{\gamma_1}{\sqrt{-\alpha_2 \alpha_3}} \frac{1}{\dot{\gamma}}$ (see *SI Appendix* for details). Using $\alpha_2 \approx -1.66$ Pa·s and $\alpha_3 \approx 0.03$ Pa·s (59), we observe a good agreement with τ_1 from our experiments, as shown by the black line in Fig. 4C. This shows that the fluctuations of the pure-twist disclination loops are a direct reflection of the tumbling dynamics of the director.

Conclusions

Our studies reveal the emergence of pure-twist disclination loops in a range of intermediate shear rates in pressure-driven flow

of nematic DSCG solutions. The disclination loops form at the boundary between two regions of irreconcilable director alignments. Their nucleation releases the high elastic stresses of the director gradient at the boundary, which induces twist-type defects because of the low elastic cost associated with the twist mode compared to splay and bend modes in DSCG solutions. By controlling the shear rate, we can tune both the size and the dynamics of the pure-twist disclination loops, which could provide guidelines for using flowing LCLCs to guide the assembly of active matter or particles (18). We demonstrate the power of PSIM in unraveling fluctuations of defects, which may also enable investigations of the dynamics of other nonequilibrium systems, including active nematics or turbulent elongated cells (55, 66, 67).

Materials and Methods

Experimental Methods. We dissolve DSCG (TCI America; purity > 98.0%) at 13.0 wt% in deionized water. The sample is sealed in a glass tube and heated until it reaches the isotropic phase, indicated by a turbidity change from turbid to transparent. The sample is subsequently cooled to room temperature (22.5 ± 0.5 °C), where it is in the nematic phase (59, 60). The rectangular microfluidic channel consists of two glass plates separated by 6.5 ± 1 μm spacers. To ensure a well-controlled initial condition of the liquid crystal, we use a protocol of surface rubbing, which induces a planar alignment of DSCG along the direction of the flow, where both glass plates are rubbed along the cell length direction using diamond particles of diameter ≈ 50 nm (68).

After injecting the sample in the microfluidic channel, we allow it to relax for 1 h, until it appears black when imaged through crossed polarizers, where one polarizer is placed parallel to the channel direction. The flow is controlled by a syringe pump (Harvard PHD 2000) set to a volumetric flow rate q ranging between $q = 0.07$ – 25 μL/min. Once the flow has reached steady state, we image the sample at the center line of the channel at a frame rate of 506 frames per second in a 250×250 μm² region far from the inlet (20–30 mm) to avoid artifacts due to the injection protocol. At the lowest flow rate (0.07 μL/min), we start the measurement 40–50 min after the onset of flow. At intermediate flow rates (0.1–0.5 μL/min), we start the measurement after 15–20 min. At higher flow rates (1–25 μL/min), we start the measurement after 5–10 min. These times are well within the steady-state regime, as determined in additional experiments.

Numerical Methods. We adopt a hybrid lattice Boltzmann method to simulate the pressure-driven flow of nematic DSCG solutions. This method has been used in prior studies of passive and active lyotropic nematics (16, 37, 69–71). The nematic is described by a symmetric and traceless tensorial order parameter, defined as follows (64):

$$\mathbf{Q} = S(\mathbf{n}\mathbf{n} - \mathbf{I}/3), \quad [8]$$

where S is the scalar order parameter, \mathbf{n} is the unit vector representing the local nematic orientation, and \mathbf{I} is an identity tensor. The governing Beris–Edwards equation of the nematic microstructure (9) reads as follows (72):

$$(\partial_t + \mathbf{u} \cdot \nabla) \mathbf{Q} - \mathbf{S}(\mathbf{W}, \mathbf{Q}) = \Gamma \mathbf{H}, \quad [9]$$

where \mathbf{u} is the velocity vector and Γ is related to the rotational viscosity of the nematic γ_1 via $\Gamma = 2S_0^2/\gamma_1$, with S_0 the equilibrium scalar order parameter. The generalized advection term $\mathbf{S}(\mathbf{W}, \mathbf{Q})$ is defined as follows:

$$\begin{aligned} \mathbf{S}(\mathbf{W}, \mathbf{Q}) = & (\xi \mathbf{A} + \Omega)(\mathbf{Q} + \mathbf{I}/3) + (\mathbf{Q} + \mathbf{I}/3)(\xi \mathbf{A} - \Omega) \\ & - 2\xi(\mathbf{Q} + \mathbf{I}/3)\text{Tr}(\mathbf{Q}\mathbf{A}), \end{aligned} \quad [10]$$

where $\mathbf{A} = (\nabla \mathbf{u} + (\nabla \mathbf{u})^T)/2$ is the strain rate tensor, $\Omega = (\nabla \mathbf{u} - (\nabla \mathbf{u})^T)/2$ is the vorticity, and ξ is a flow-alignment parameter. Here, we choose $\xi < 3S_0/(2 + S_0)$ to enter a flow-tumbling regime (73). The molecular field \mathbf{H} is a symmetric, traceless projection of the functional derivative of the free energy of the nematic. Its index form reads as follows:

$$H_{ij} = \frac{1}{2} \left(\frac{\delta F}{\delta Q_{ij}} + \frac{\delta F}{\delta Q_{ji}} \right) - \frac{\delta_{ij}}{3} \text{Tr} \left(\frac{\delta F}{\delta Q_{ij}} \right), \quad [11]$$

in which the free energy functional is $F = \int_V f dV$. The density f consists of a short-range Landau–de Gennes component and a long-range elastic component (74):

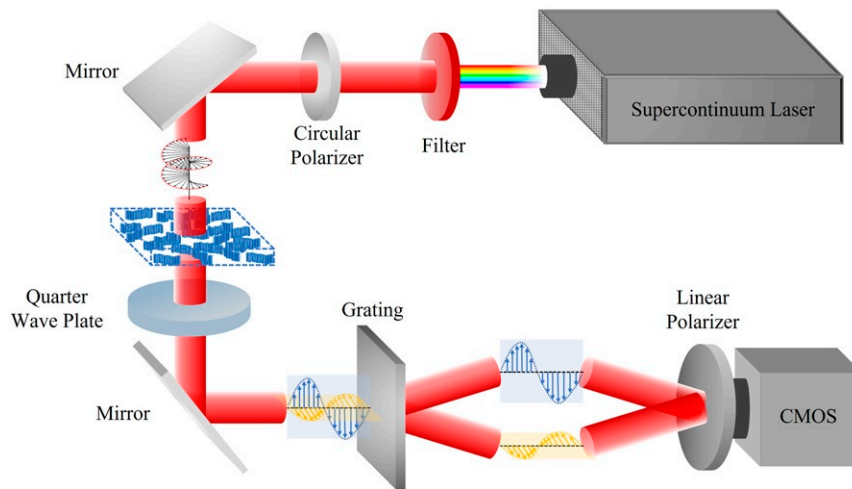


Fig. 5. Schematic diagram of polarized shearing interference microscopy (PSIM). The filter is a bandpass filter centered at wavelength 633 nm with bandwidth 10 nm.

$$f = \frac{A_0}{2} \left(1 - \frac{U}{3} \right) Q_{ij} Q_{ij} - \frac{A_0 U}{3} Q_{ij} Q_{jk} Q_{ki} + \frac{A_0 U}{4} (Q_{ij} Q_{ij})^2 + \frac{1}{2} L_1 Q_{ij,k} Q_{ij,k} + \frac{1}{2} L_2 Q_{jk,k} Q_{ij,l} + \frac{1}{2} L_3 Q_{ij} Q_{kl,i} Q_{kl,j} + \frac{1}{2} L_4 Q_{jk,i} Q_{jl,k}, \quad [12]$$

where A_0 and U are material constants, $Q_{ij,k}$ denotes $\partial_k Q_{ij}$, and L_1 to L_4 are related to the Frank elastic constants through the following (71):

$$\begin{aligned} L_1 &= \frac{1}{2S_0^2} \left[K_2 + \frac{1}{3} (K_3 - K_1) \right], \\ L_2 &= \frac{1}{S_0^2} (K_1 - K_{24}), \\ L_3 &= \frac{1}{2S_0^2} (K_3 - K_1), \\ L_4 &= \frac{1}{S_0^2} (K_{24} - K_2), \end{aligned} \quad [13]$$

where K_1 , K_2 , K_3 , and K_{24} denote the splay, twist, bend, and saddle-splay Frank elastic constants, respectively. Eq. 9 is solved using a finite difference method.

The hydrodynamic flow is governed by a momentum equation (73, 75, 76):

$$\rho(\partial_t + u_j \partial_j) u_i = \partial_j \Pi_{ij} + \eta \partial_j [\partial_i u_j + \partial_j u_i + (1 - 3\partial_\rho P_0) \partial_\gamma u_\gamma \delta_{ij}], \quad [14]$$

where ρ is the density, η is the isotropic viscosity, and $P_0 = \rho T - f$ is the hydrostatic pressure with T being the temperature. The additional stress accounting for the nematic anisotropy is defined as follows (73, 75, 76):

$$\begin{aligned} \Pi_{ij} &= -P_0 \delta_{ij} - \xi H_{ik} \left(Q_{kj} + \frac{1}{3} \delta_{kj} \right) \\ &\quad - \xi \left(Q_{ik} + \frac{1}{3} \delta_{ik} \right) H_{kj} \\ &\quad + 2\xi \left(Q_{ij} + \frac{1}{3} \delta_{ij} \right) Q_{kl} H_{kl} \\ &\quad - \partial_j Q_{kl} \frac{\delta F}{\delta \partial_j Q_{kl}} + Q_{ik} H_{kj} - H_{ik} Q_{kj}. \end{aligned} \quad [15]$$

Eq. 14 is solved simultaneously via a lattice Boltzmann method over a D3Q15 grid (75). The simulation is performed in a rectangular box $[X, Y, Z] = [150, 150, 50]$ in simulation units with periodic boundary conditions in the x and y directions, and no-slip and planar anchoring condition in the z direction. A body force $g \in [2.5 \times 10^{-5} - 5 \times 10^{-3}]$ is applied to generate a pressure-driven flow. Additional details on this method can be found in ref. 76. Typical simulation parameters are $\Gamma = 0.1$, $\eta = 0.33$, $A = 0.01$, $U = 3.5$ corresponding to $S_0 \sim 0.62$, $\xi = 0.6$ giving rise to $\alpha_3/\alpha_2 = -0.08$, and $[L_1, L_2, L_3, L_4] = [0.01, 0, 0.03247, 0.01333]$ leading to $K_1 : K_2 : K_3 : K_{24} = 1 : 0.33 : 3 : 1$.

PSIM. The optical design of PSIM is based on the combination of off-axis shearing interferometry and circular polarization microscopy, as shown in Fig. 5. A supercontinuum laser serves as the illumination source with center wavelength at 633 nm set by a bandpass filter with a 10-nm pass band. The excitation is transmitted through a quarter waveplate to produce circular polarization light before impinging on the birefringent sample. The scattered light is then collected by a microscope and transmitted through a second quarter wave plate to transform the electric field's polarization states back to linear polarization. The electric field component parallel and perpendicular to the slow axis of the quarter wave plate encode specimen birefringence information. To quantify the ratio of these two electric field components, the image is duplicated by a diffraction grating, each polarization component is selected by a linear polarizer at the Fourier plane, and they are recombined after a linear polarizer set at 45° to form an interferogram on the CMOS camera.

In the interferogram, interference fringes will only appear in the region that has birefringent signals. The retrieval of the optical retardance is thus related to the extraction of the interference fringe's amplitude. Similar to quantitative phase microscopy (77), we extract the amplitude of the retrieved +1 order E , along with the amplitude of the DC term A from the interferograms with a digital holography algorithm. The retardance Γ is extracted as follows:

$$\Gamma = \sin^{-1} \left(\frac{2E}{A} \right). \quad [16]$$

This straightforward polarization parameter retrieval algorithm avoids the amplification of noise while quantitatively mapping the retardance from a single interferogram.

During image processing, we down-sample each frame by a factor of 10 ($1,200 \times 1,200$ pixels to 120×120 pixels) to reduce the data size. This significantly increases the processing speed, but negligibly affects the information retrieved from the images as the down-sampled pixel size is still comparable to the diffraction limit (the diffraction limit is $1.54 \mu\text{m}$, the down-sampled pixel size is $2.08 \times 2.08 \mu\text{m}^2$). The time interval between two consecutive frames is 1.97 ms.

Data Availability. All study data are included in the article and/or supporting information.

ACKNOWLEDGMENTS. We thank Žiga Kos and Shuang Zhou for helpful discussions. Q.Z. and I.B. acknowledge support from the Massachusetts Institute of Technology (MIT) Research Support Committee. B.G., Z.Y., and P.T.C.S. acknowledge support from NIH Grants 5-P41-EB015871-27 and 5R21NS091982-02, and the Hamamatsu Corporation. B.G. and P.T.C.S. acknowledge support from the Singapore-MIT Alliance for Research and Technology Center, Critical Analytics for Manufacturing Personalized-Medicine Interdisciplinary Research Group. Z.Y. and P.T.C.S. acknowledge support from NIH Grants R01DA045549 and R21GM140613-02. B.G. acknowledges support from a Mathworks Fellowship. R.Z. acknowledges support from the Hong Kong Research Grants Council Grant 26302320.

1. H. S. Park *et al.*, Self-assembly of lyotropic chromonic liquid crystal Sunset Yellow and effects of ionic additives. *J. Phys. Chem. B* **112**, 16307–16319 (2008).
2. M. P. Renshaw, I. J. Day, NMR characterization of the aggregation state of the azo dye sunset yellow in the isotropic phase. *J. Phys. Chem. B* **114**, 10032–10038 (2010).
3. J. Lydon, Chromonic liquid crystalline phases. *Liq. Cryst.* **38**, 1663–1681 (2011).
4. S. Zhou *et al.*, Elasticity of lyotropic chromonic liquid crystals probed by director reorientation in a magnetic field. *Phys. Rev. Lett.* **109**, 037801 (2012).
5. S. Zhou *et al.*, Elasticity, viscosity, and orientational fluctuations of a lyotropic chromonic nematic liquid crystal disodium cromoglycate. *Soft Matter* **10**, 6571–6581 (2014).
6. P. J. Collings *et al.*, The nature of the assembly process in chromonic liquid crystals. *Liq. Cryst. Rev.* **3**, 1–27 (2015).
7. S. V. Shiyankovskii *et al.*, Lyotropic chromonic liquid crystals for biological sensing applications. *Mol. Cryst. Liq. Cryst. (Phila. Pa.)* **434**, 259–587 (2005).
8. T. Sergan, T. Schneider, J. Kelly, O. D. Lavrentovich, Polarizing-alignment layers for twisted nematic cells. *Liq. Cryst.* **27**, 567–572 (2000).
9. S. W. Tam-Chang, W. Seo, K. Rove, S. M. Casey, Molecularly designed chromonic liquid crystals for the fabrication of broad spectrum polarizing materials. *Chem. Mater.* **16**, 1832–1834 (2004).
10. V. G. Nazarenko *et al.*, Lyotropic chromonic liquid crystal semiconductors for water-solution processable organic electronics. *Appl. Phys. Lett.* **97**, 284 (2010).
11. F. Guo, A. Mukhopadhyay, B. W. Sheldon, R. H. Hurt, Vertically aligned graphene layer arrays from chromonic liquid crystal precursors. *Adv. Mater.* **23**, 508–513 (2011).
12. H. S. Park, O. D. Lavrentovich, *Liquid Crystals Beyond Displays: Chemistry, Physics, and Applications* (Wiley, 2012).
13. S. Zhou, A. Sokolov, O. D. Lavrentovich, I. S. Aranson, Living liquid crystals. *Proc. Natl. Acad. Sci. U.S.A.* **111**, 1265–1270 (2014).
14. A. Masters, Chromonic liquid crystals: More questions than answers. *Liq. Cryst. Today* **25**, 30–37 (2016).
15. M. M. Genkin, A. Sokolov, O. D. Lavrentovich, I. S. Aranson, Topological defects in a living nematic ensnare swimming bacteria. *Phys. Rev. X* **7**, 011029 (2017).
16. A. Sokolov, A. Mozaffari, R. Zhang, J. J. De Pablo, A. Snezhko, Emergence of radial tree of bend stripes in active nematics. *Phys. Rev. X* **9**, 031014 (2019).
17. P. C. Mushenheim *et al.*, Effects of confinement, surface-induced orientations and strain on dynamical behaviors of bacteria in thin liquid crystalline films. *Soft Matter* **11**, 6821–6831 (2015).
18. C. Peng, T. Turiv, Y. Guo, Q. H. Wei, O. D. Lavrentovich, Command of active matter by topological defects and patterns. *Science* **354**, 882–885 (2016).
19. S. Zhou *et al.*, Dynamic states of swimming bacteria in a nematic liquid crystal cell with homeotropic alignment. *New J. Phys.* **19**, 055006 (2017).
20. C. Peng *et al.*, Control of colloidal placement by modulated molecular orientation in nematic cells. *Sci. Adv.* **2**, e1600932 (2016).
21. I. Janossy, P. Pieranski, E. Guyon, Poiseuille flow in nematics: Experimental study of the instabilities. *J. Phys. (Paris)* **37**, 1105–1113 (1976).
22. D. J. Graziano, M. R. Mackley, Shear induced optical textures and their relaxation behaviour in thermotropic liquid crystalline polymers. *Mol. Cryst. Liq. Cryst. (Phila. Pa.)* **106**, 73–93 (1984).
23. J. Vermant, P. Moldenaers, S. J. Picken, J. Mewis, A comparison between texture and rheological behaviour of lyotropic liquid crystalline polymers during flow. *J. Non-Newton. Fluid Mech.* **53**, 1–23 (1994).
24. P. T. Mather, D. S. Pearson, R. G. Larson, Flow patterns and disclination-density measurements in sheared nematic liquid crystals I: Flow-aligning 5CB. *Liq. Cryst.* **20**, 527–538 (1996).
25. R. G. Larson, *The Structure and Rheology of Complex Fluids* (Oxford University Press, 1999).
26. J. A. Müller, R. S. Stein, H. H. Winter, Rotation of liquid crystalline macromolecules in shear flow and shear-induced periodic orientation patterns. *Rheol. Acta* **35**, 160–167 (1996).
27. A. Sengupta *et al.*, Liquid crystal microfluidics for tunable flow shaping. *Phys. Rev. Lett.* **110**, 048303 (2013).
28. A. D. Rey, M. M. Denn, Dynamical phenomena in liquid-crystalline materials. *Annu. Rev. Fluid Mech.* **34**, 233–266 (2002).
29. D. H. Klein, L. G. Leal, C. J. García-Cervera, H. D. Ceniceros, Three-dimensional shear-driven dynamics of polydomain textures and disclination loops in liquid crystalline polymers. *J. Rheol.* **52**, 837–863 (2008).
30. M. Kleman, O. D. Lavrentovich, *Soft Matter Physics: An Introduction* (Springer Science and Business Media, 2007).
31. D. J. Graziano, M. R. Mackley, Disclinations observed during the shear of MBBA. *Mol. Cryst. Liq. Cryst. (Phila. Pa.)* **106**, 103–119 (1984).
32. A. Sengupta, B. Schulz, E. Ouskova, C. Bahr, Functionalization of microfluidic devices for investigation of liquid crystal flows. *Microfluid. Nanofluidics* **13**, 941–955 (2012).
33. Z. Liu, D. Luo, K. L. Yang, Flow-driven disclination lines of nematic liquid crystals inside a rectangular microchannel. *Soft Matter* **15**, 5638–5643 (2019).
34. A. Sengupta, U. Tkalec, C. Bahr, Nematic textures in microfluidic environment. *Soft Matter* **7**, 6542–6549 (2011).
35. H. Agha, C. Bahr, Connecting and disconnecting nematic disclination lines in microfluidic channels. *Soft Matter* **12**, 4266–4273 (2016).
36. L. Gioni, Ž. Kos, M. Ravnik, A. Sengupta, Cross-talk between topological defects in different fields revealed by nematic microfluidics. *Proc. Natl. Acad. Sci. U.S.A.* **114**, E5771–E5777 (2017).
37. T. Emeršič *et al.*, Sculpting stable structures in pure liquids. *Sci. Adv.* **5**, eaav4283 (2019).
38. S. Čopar, Ž. Kos, T. Emeršič, U. Tkalec, Microfluidic control over topological states in channel-confined nematic flows. *Nat. Commun.* **11**, 59 (2020).
39. T. Ouchi, K. Imamura, K. Sunami, H. Yoshida, M. Ozaki, Topologically protected generation of stable wall loops in nematic liquid crystals. *Phys. Rev. Lett.* **123**, 097801 (2019).
40. T. De'Nève, P. Navard, M. Kleman, Nature of the flow-induced worm texture of thermotropic polymers. *Macromolecules* **28**, 1541–1546 (1995).
41. M. Doi, S. F. Edwards, *The Theory of Polymer Dynamics* (Oxford University Press, 1988).
42. G. Marrucci, F. Greco, Flow behavior of liquid crystalline polymers. *Adv. Chem. Phys.* **86**, 331–404 (1993).
43. G. Sgalari, G. L. Leal, J. J. Feng, The shear flow behavior of LCPs based on a generalized Doi model with distortional elasticity. *J. Non-Newton. Fluid Mech.* **102**, 361–382 (2002).
44. H. Baza *et al.*, Shear-induced polydomain structures of nematic lyotropic chromonic liquid crystal disodium cromoglycate. *Soft Matter* **16**, 8565–8576 (2020).
45. A. Sharma, I. L. H. Ong, A. Sengupta, Time dependent lyotropic chromonic textures in microfluidic confinements. *Crystals (Basel)* **11**, 35 (2021).
46. S. Zhou, S. V. Shiyankovskii, H. S. Park, O. D. Lavrentovich, Fine structure of the topological defect cores studied for disclinations in lyotropic chromonic liquid crystals. *Nat. Commun.* **8**, 14974 (2017).
47. K. Nayani *et al.*, Spontaneous emergence of chirality in achiral lyotropic chromonic liquid crystals confined to cylinders. *Nat. Commun.* **6**, 8067 (2015).
48. Z. S. Davidson *et al.*, Chiral structures and defects of lyotropic chromonic liquid crystals induced by saddle-splay elasticity. *Phys. Rev. E Stat. Nonlin. Soft Matter Phys.* **91**, 050501 (2015).
49. L. Tortora, O. D. Lavrentovich, Chiral symmetry breaking by spatial confinement in tactoidal droplets of lyotropic chromonic liquid crystals. *Proc. Natl. Acad. Sci. U.S.A.* **108**, 5163–5168 (2011).
50. G. Park *et al.*, Periodic arrays of chiral domains generated from the self-assembly of micropatterned achiral lyotropic chromonic liquid crystal. *ACS Cent. Sci.* **6**, 1964–1970 (2020).
51. O. D. Lavrentovich, Design of chiral domains by surface confinement of liquid crystals. *ACS Cent. Sci.* **6**, 1858–1861 (2020).
52. K. V. Kaznatcheev, P. Dudin, O. D. Lavrentovich, A. P. Hitchcock, X-ray microscopy study of chromonic liquid crystal dry film texture. *Phys. Rev. E Stat. Nonlin. Soft Matter Phys.* **76**, 061703 (2007).
53. T. Suzuki, Y. Kojima, Direct structural observation of the alignment and elongation in lyotropic chromonic liquid crystals under shear flow. *Mol. Cryst. Liq. Cryst. (Phila. Pa.)* **648**, 162–167 (2017).
54. Y. J. Cha *et al.*, Orthogonal liquid crystal alignment layer: Templating speed-dependent orientation of chromonic liquid crystals. *ACS Appl. Mater. Interfaces* **9**, 18355–18361 (2017).
55. G. Duclos *et al.*, Topological structure and dynamics of three-dimensional active nematics. *Science* **367**, 1120–1124 (2020).
56. I. I. Smalyukh, S. V. Shiyankovskii, O. D. Lavrentovich, Three-dimensional imaging of orientational order by fluorescence confocal polarizing microscopy. *Chem. Phys. Lett.* **336**, 88–96 (2001).
57. M. Shribak, R. Oldenbourg, Techniques for fast and sensitive measurements of two-dimensional birefringence distributions. *Appl. Opt.* **42**, 3009–3017 (2003).
58. B. Ge *et al.*, Single-shot quantitative polarization imaging of complex birefringent structure dynamics. *arXiv [Preprint]* (2021). <https://arxiv.org/abs/2106.06118> (Accessed 11 June 2021).
59. S. Zhou, “Elasticity, viscosity, and orientational fluctuations of a lyotropic chromonic nematic liquid crystal disodium cromoglycate” in *Lyotropic Chromonic Liquid Crystals: From Viscoelastic Properties to Living Liquid Crystals* (Springer, 2017), pp. 51–75.
60. N. Zimmermann, G. Jünemann-Held, P. J. Collings, H. S. Kitzerow, Self-organized assemblies of colloidal particles obtained from an aligned chromonic liquid crystal dispersion. *Soft Matter* **11**, 1547–1553 (2015).
61. Y. A. Nastishin *et al.*, Optical characterization of the nematic lyotropic chromonic liquid crystals: Light absorption, birefringence, and scalar order parameter. *Phys. Rev. E Stat. Nonlin. Soft Matter Phys.* **72**, 041711 (2005).
62. P. Manneville, Non-linearities and fluctuations at the threshold of a hydrodynamic instability in nematic liquid crystals. *J. Phys. (Paris)* **39**, 911–925 (1978).
63. Q. Ouyang, H. L. Swinney, Transition to chemical turbulence. *Chaos* **1**, 411–420 (1991).
64. P. G. De Gennes, J. Prost, *The Physics of Liquid Crystals* (Oxford University Press, 1993).
65. D. Grecov, A. D. Rey, Shear-induced textural transitions in flow-aligning liquid crystal polymers. *Phys. Rev. E Stat. Nonlin. Soft Matter Phys.* **68**, 061704 (2003).
66. C. Blanch-Mercader *et al.*, Turbulent dynamics of epithelial cell cultures. *Phys. Rev. Lett.* **120**, 208101 (2018).
67. A. Doostmohammadi, J. Ignés-Mullol, J. M. Yeomans, F. Sagués, Active nematics. *Nat. Commun.* **9**, 3246 (2018).
68. L. Parry-Jones, *Alignment Properties of Liquid Crystals in Handbook of Visual Display Technology* (Springer, 2016), pp. 2003–2020.
69. R. Zhang, Y. Zhou, M. Rahimi, J. J. de Pablo, Dynamic structure of active nematic shells. *Nat. Commun.* **7**, 13483 (2016).
70. R. Zhang, N. Kumar, J. L. Ross, M. L. Gardel, J. J. de Pablo, Interplay of structure, elasticity, and dynamics in actin-based nematic materials. *Proc. Natl. Acad. Sci. U.S.A.* **115**, E124–E133 (2018).

71. N. Kumar, R. Zhang, J. J. de Pablo, M. L. Gardel, Tunable structure and dynamics of active liquid crystals. *Sci. Adv.* **4**, eaat7779 (2018).
72. A. N. Beris, B. J. Edwards, *Thermodynamics of Flowing Systems with Internal Microstructure* (Oxford University Press, 1994).
73. C. Denniston, E. Orlandini, J. M. Yeomans, Lattice Boltzmann simulations of liquid crystal hydrodynamics. *Phys. Rev. E Stat. Nonlin. Soft Matter Phys.* **63**, 056702 (2001).
74. M. Ravnik, S. Žumer, Landau-de Gennes modelling of nematic liquid crystal colloids. *Liq. Cryst.* **36**, 1201–1214 (2009).
75. C. Denniston, D. Marenduzzo, E. Orlandini, J. M. Yeomans, Lattice Boltzmann algorithm for three-dimensional liquid-crystal hydrodynamics. *Philos. Trans. R. Soc. Lond. A Math. Phys. Eng. Sci.* **362**, 1745–1754 (2004).
76. R. Zhang, T. Roberts, I. S. Aranson, J. J. de Pablo, Lattice Boltzmann simulation of asymmetric flow in nematic liquid crystals with finite anchoring. *J. Chem. Phys.* **144**, 084905 (2016).
77. Y. Park, C. Depeursinge, G. Popescu, Quantitative phase imaging in biomedicine. *Nat. Photonics* **12**, 578–589 (2018).